Finite Control Set Model Predictive Current Control for Grid-Connected Voltage-Source Converters With *LCL* Filters: A Study Based on Different State Feedbacks

Niklas Panten, Nils Hoffmann, *Member, IEEE*, and Friedrich Wilhelm Fuchs, *Senior Member, IEEE*

***Abstract*—This paper presents different state feedback approaches of finite control set model predictive control (FCS-MPC) applied to a grid-connected voltage-source converter (VSC) with an *LCL* filter. Besides converter-side current feedback, two multivariable control approaches and line-side current control are introduced and compared based on theoretical and experimental evaluation. As the *LCL* filter introduces an additional resonance frequency to the system, the use of different active damping (AD) methods in combination with FCS-MPC is discussed. Furthermore, practical control implementation issues are discussed. The presented methods reveal the great potential, high dynamic performance, and flexibility of FCS-MPC, enabling multivariable control as well as both reduced switching losses and low harmonic current distortion at the same time. Eventually, the feasibility of the theoretical control concepts is shown in a laboratory environment.**

***Index Terms*—Active damping (AD), digital control, direct current control, finite control set (FCS), grid-connected converter, *LCL* filter, model predictive control (MPC), state feedback, voltage-source converter (VSC).**

I. Introduction

THE total installed power of voltage-source converters (VSCs) that are connected to the power grid has experienced a dramatic growth during the last decades [1] and which will no doubt continue considering the vigorous efforts of promoting decentralized renewable energy [2]. At the same time the computing speed of modern digital signal processors (DSP) has multiplied and enabled modern control strategies like fuzzy control [3], adaptive control [4], sliding mode control [5] or predictive control algorithms [6]–[13] to be applied in industrial power electronic converter systems.

Recently, model predictive control (MPC) [14]–[21] has been demonstrated to be a promising alternative to classical pulsewidth modulation (PWM) control schemes based on voltage-oriented control (VOC) [22] or direct power control (DPC) [23]. In contrast to continuous control set MPC (CCS-MPC), the finite control set (or direct) MPC (FCS-MPC) scheme does not need a modulator and is well designed for digital power inverter control systems that are characterized by discrete sampling values, well-known models, nonlinearities, a finite number of switching states, and additional physical system constraints. FCS-MPC meets those requirements and offers great flexibility for various power converting applications, as highlighted in [6]. Additionally, this control scheme allows variable switching frequencies. Consequently, FCS-MPC provides the potential to optimize switching power losses and their distribution in complex converter topologies by directly manipulating the semiconductors switching states [24], [25]. However, MPC algorithms put large requirements on the control hardware in terms of computation performance and speed [26].

Moreover, the high-frequency switching transitions (typically 2–15 kHz for low-voltage medium/high-power applications) cause high-order harmonics, which can disturb sensitive equipment connected to the grid [27]. In order to fulfill the grid code requirements, it is necessary to introduce a line filter between the VSC and the point of common coupling (PCC). FCS-MPC has been proven to suit well for simple inductive filters (*L* filters), e.g., presented in [8]–[11]. However, an *LCL* filter is an attractive alternative to reduce costs and improve dynamic response compared to conventional *L* filters [27], [28]. This third-order filter embodies a substantially more complex control problem as resonance frequencies may get excited by switching harmonics. To achieve sinusoidal line currents with low total harmonic distortion (THD), this problem has to be addressed by adequate filter design and active damping (AD) strategies [29]. Typically, FCS-MPC leads to variable switching frequencies. Thus, special attention has to be paid while introducing AD methods to FCS-MPC applications, such as suggested in [30]–[32].

In this paper, online optimized FCS-MPC approaches for grid-connected VSC with *LCL* filters based on different state feedbacks are presented with the objective to minimize switching losses (via lower switching frequencies) and achieve acceptable current distortion. Besides common converter-side current

Manuscript received March 14, 2015; revised June 2, 2015 and August 8, 2015; accepted August 31, 2015. Date of publication September 22, 2015; date of current version January 28, 2016. This work was supported in part by the Ministry of Schleswig-Holstein, Germany, in part by the European Union, and in part by the CEwind e.G. Center of Excellence for wind energy in Schleswig-Holstein. Recommended for publication by Associate Editor Q.-C. Zhong.

N. Panten was with the Institute of Power Electronics and Electrical Drives, Christian-Albrechts-University of Kiel, Kiel D-24143, Germany. He is now with the Institute for Production Management, Technology and Machine Tools (PTW), Technical University of Darmstadt, Darmstadt, Germany (e-mail: niklas@panten.eu).

N. Hoffmann is with the Department for Research and Product Development, Ingenieurbüro Hoffmann GmbH, Halle/Saale D-06188, Germany (e-mail: nils.hoffmann@ibrhoffmann.de).

F. W. Fuchs is with the Institute of Power Electronics and Electrical Drives, Christian-Albrechts-University of Kiel, Kiel D-24143, Germany (e-mail: fwf@tf.uni.kiel.de).

Color versions of one or more of the figures in this paper are available online at http://ieeexplore.ieee.org.

Digital Object Identifier 10.1109/TPEL.2015.2478862

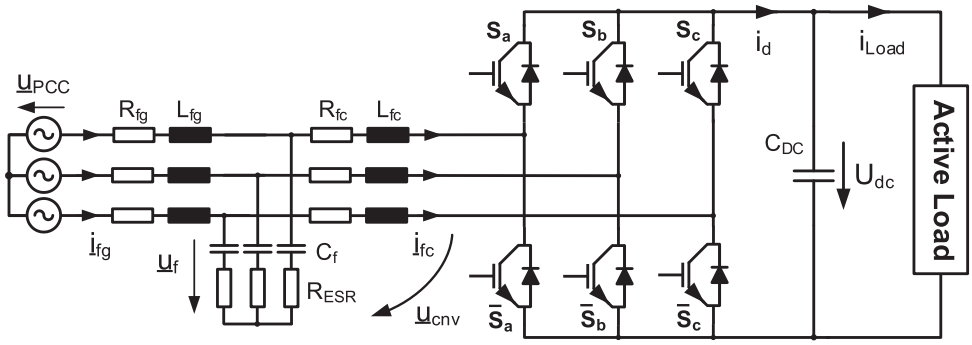

Fig. 1. Block diagram of grid-connected VSC with *LCL* filter.

feedback, this paper presents and compares three new feedback approaches including multivariable control and direct line-side current control based on FCS-MPC. To overcome stability issues and avoid excitation of the *LCL* filter natural frequencies, AD approaches are discussed. Among well-known virtual-resistance AD, an approach by additional control variables and model-based long-term prediction AD are studied. Measurements are carried out utilizing a 22-kW laboratory test-bench that includes a grid-connected two-level VSC with an *LCL*-type line filter.

This paper is structured as follows: In Section II, a description of the system and the key aspects of proper system modeling and discretization are given. Following this, the general concept of FCS-MPC and advanced features, like switching frequency reduction or algorithm optimization for a reduced calculation burden, are introduced in Section III. The studies on the *LCL* filter control problem and different feedback approaches with AD solutions are compared and further discussed in Section IV. To validate the theoretical concept, Section V presents an experimental analysis.

II. System Modeling

As its name implies, MPC utilizes a system model. Therefore, proper system modeling and discretization are key elements for a successful implementation and satisfying control performance. The system variables of the system under study are illustrated in Fig. 1. The system model is based on the stationary $\alpha\beta$ reference frame representation. For a balanced three-phase system with isolated neutral point, the zero sequence components are neglected. Thus, all generic three-phase variables $\boldsymbol{z_{abc}} \in \mathbb{R}^3$ are transformed to $\boldsymbol{z_{\alpha\beta}} \in \mathbb{R}^2$ by applying the simplified, amplitude-invariant Clarke transformation as given in (1). The two-dimensional vector $\boldsymbol{z_{\alpha\beta}}$ is equally expressed as the complex variable $\underline{z}_{\alpha\beta}$ with the complex transformation matrix $\underline{\boldsymbol{T}}_{\boldsymbol{\alpha\beta}}$ (2)

$$\boldsymbol{z_{\alpha\beta}} = \begin{bmatrix} z_\alpha \\ z_\beta \end{bmatrix} = \boldsymbol{T_{\alpha\beta}} \boldsymbol{z_{abc}}, \quad \boldsymbol{T_{\alpha\beta}} = \frac{1}{3} \begin{bmatrix} 2 & -1 & -1 \\ 0 & \sqrt{3} & -\sqrt{3} \end{bmatrix} \tag{1}$$

$$\underline{z}_{\alpha\beta} = z_\alpha + j z_\beta = \underline{T}_{\boldsymbol{\alpha\beta}} \boldsymbol{z_{abc}}, \quad \underline{\boldsymbol{T}}_{\boldsymbol{\alpha\beta}} = \frac{2}{3} \begin{bmatrix} 1 & e^{j\frac{2}{3}\pi} & e^{j\frac{4}{3}\pi} \end{bmatrix}. \tag{2}$$

A. LCL Filter

The converter-side current i_{fc} is defined as the current through the converter-side filter inductance L_{fc} and the associated winding resistance R_{fc}. On the other side, i_{fg} represents the current through line-side inductance L_{fg} and winding resistance R_{fg}. Furthermore, u_f is defined as the voltage across the filter capacitance C_f and equivalent serial resistance R_f. By applying Kirchhoff's law to the *LCL* filter elements and rearranging the equations, a state-space model is derived with the state vector $\boldsymbol{x}_1$, system matrix $\boldsymbol{A}_1$ and control matrix $\boldsymbol{B}_1$, as specified in (3)-(5). The system states are influenced by the control vector $\boldsymbol{u}_1$, consisting of the converter output voltage $\underline{u}_{cnv}$ as the control variable and the disturbance voltage $\underline{u}_{\mathrm{PCC}}$ at the PCC

$$\underbrace{\frac{d}{dt}\begin{bmatrix} \underline{i}_{fc}(t) \\ \underline{i}_{fg}(t) \\ \underline{u}_f(t) \end{bmatrix}}_{\dot{\boldsymbol{x}}_1} = \boldsymbol{A}_1 \underbrace{\begin{bmatrix} \underline{i}_{fc}(t) \\ \underline{i}_{fg}(t) \\ \underline{u}_f(t) \end{bmatrix}}_{\boldsymbol{x}_1} + \boldsymbol{B}_1 \underbrace{\begin{bmatrix} \underline{u}_{cnv}(t) \\ \underline{u}_{\mathrm{pcc}}(t) \end{bmatrix}}_{\boldsymbol{u}_1} \tag{3}$$

$$\boldsymbol{A}_1 = \begin{bmatrix} -\dfrac{R_{fc}}{L_{fc}} & 0 & \dfrac{1}{L_{fc}} \\ 0 & -\dfrac{R_{fg}}{L_{fg}} & -\dfrac{1}{L_{fg}} \\ \dfrac{R_f R_{fc}}{L_{fc}} - \dfrac{1}{C_f} & \dfrac{1}{C_f} - \dfrac{R_f R_{fg}}{L_{fg}} & -R_f\left(\dfrac{1}{L_{fc}} + \dfrac{1}{L_{fg}}\right) \end{bmatrix} \tag{4}$$

$$\boldsymbol{B}_1 = \begin{bmatrix} -\dfrac{1}{L_{fc}} & 0 & \dfrac{R_f}{L_{fc}} \\ 0 & \dfrac{1}{L_{fg}} & \dfrac{R_f}{L_{fg}} \end{bmatrix}^T. \tag{5}$$

B. Converter and DC Link

Given the 2^3 switching states of a three-phase two-level VSC, an ideal switch model with either active upper ($s = 1$) or active lower half bridge ($s = -1$) is used as described in (6). As a consequence, with respect to the virtual neutral point *N*, either the electrical potential $+u_{\mathrm{dc}}/2$ or $-u_{\mathrm{dc}}/2$ is applied to the corresponding ac-side phase output terminals of the converter.

Utilizing the Clarke transformation, the three-phase converter output voltage $\underline{u}_{cnv}$ is expressed as a function of the switching vector $\boldsymbol{s}$, cf. (7)

$$\boldsymbol{s}(t) = \begin{bmatrix} s_a(t) \\ s_b(t) \\ s_c(t) \end{bmatrix}, \quad \boldsymbol{s}(t) \in \mathcal{S} = \{1,-1\}^3 \,\forall t \tag{6}$$

$$\underline{u}_{\mathrm{cnv}}(t) = \underline{\boldsymbol{T}}_{\boldsymbol{\alpha\beta}} \boldsymbol{s}(t) \cdot \frac{u_{\mathrm{dc}}(t)}{2}. \tag{7}$$

For improving load disturbance rejection, the disturbance current i_{load} is added to the state-space model utilizing the dc-link current i_d (8) and the dc-link dynamics (9), leading to the state space formulation as described in (10)–(12), equation (12) is shown as the bottom of the page.

$$i_d(t) = \frac{3}{4}\left(\boldsymbol{T}_{\boldsymbol{\alpha\beta}}\boldsymbol{s}(t)\right)^T \boldsymbol{i}_{\boldsymbol{f}c,\alpha\beta}(t) \tag{8}$$

$$\frac{d}{dt}u_{\mathrm{dc}}(t) = \frac{i_d - i_{\mathrm{load}}}{C_{\mathrm{dc}}} \tag{9}$$

$$\underbrace{\frac{d}{dt}\begin{bmatrix} \underline{i}_{fc}(t) \\ \underline{i}_{fg}(t) \\ \underline{u}_f(t) \\ u_{\mathrm{dc}}(t) \\ i_{\mathrm{load}}(t) \end{bmatrix}}_{\dot{\boldsymbol{x}}_2} = \boldsymbol{A}_2[\boldsymbol{s}(t)] \underbrace{\begin{bmatrix} \underline{i}_{fc}(t) \\ \underline{i}_{fg}(t) \\ \underline{u}_f(t) \\ u_{\mathrm{dc}}(t) \\ i_{\mathrm{load}}(t) \end{bmatrix}}_{\boldsymbol{x}_2} + \boldsymbol{B}_2 \underbrace{\underline{u}_{\mathrm{pcc}}(t)}_{\boldsymbol{u}_2} \tag{10}$$

$$\boldsymbol{B}_2 = \begin{bmatrix} 0 & \dfrac{1}{L_{fg}} & \dfrac{R_f}{L_{fg}} & 0 & 0 \end{bmatrix}^T \tag{11}$$

C. PCC Voltage Disturbance

Furthermore, as the line voltages are usually unbalanced and superimposed with harmonics [33], it is advisable to improve disturbance rejection by accurate modeling [34] to ensure sinusoidal current waveforms. Therefore, the line-voltages at the PCC are modeled as multiple superimposed ac waveforms in symmetrical components

$$\begin{aligned} \underline{u}_{\mathrm{PCC}}(t) = {} & \underline{u}_{\mathrm{PCC1+}} e^{j\omega t} + \underline{u}_{\mathrm{PCC1-}} e^{-j\omega t} \\ & + \underline{u}_{\mathrm{PCC5-}} e^{-j5\omega t} + \underline{u}_{\mathrm{PCC7+}} e^{j7\omega t}. \end{aligned} \tag{13}$$

While $\underline{u}_{\mathrm{PCC1+}}$ represents the fundamental voltage positive sequence in $\alpha\beta$ coordinates, fundamental voltage unbalances are expressed by the corresponding negative voltage sequence $\underline{u}_{\mathrm{PCC1-}}$. The fifth and seventh voltage harmonics are indicated by $\underline{u}_{\mathrm{PCC5-}}$ respectively $\underline{u}_{\mathrm{PCC7+}}$, considering the corresponding positive or negative sequence in a three-phase three-wire power system [35]. The terms are added to the state space formulation as summarized in (14)–(16). The initial system values are extracted from $\underline{u}_{\mathrm{PCC}}$ with phase-locked loops based on multiple second-order generalized integrators (MSOGI-PLL) [36]

$$\frac{d}{dt}\boldsymbol{x}(t) = \boldsymbol{A}[\boldsymbol{s}(t)]\boldsymbol{x}(t) \tag{14}$$

$$\begin{aligned} \boldsymbol{x} = {} & [\underline{i}_{fc} \quad \underline{i}_{fg} \quad \underline{u}_f \quad u_{\mathrm{dc}} \quad i_{\mathrm{load}} \quad \underline{u}_{\mathrm{PCC1+}} \quad \underline{u}_{\mathrm{PCC1-}} \\ & \underline{u}_{\mathrm{PCC5-}} \quad \underline{u}_{\mathrm{PCC7+}}]^T \end{aligned} \tag{15}$$

$$\boldsymbol{A}[\boldsymbol{s}(\boldsymbol{t})] = \begin{bmatrix} \boldsymbol{A}_2[\boldsymbol{s}(t)] & \boldsymbol{B}_2 & \boldsymbol{B}_2 & \boldsymbol{B}_2 & \boldsymbol{B}_2 \\ 0 & \mathrm{j}\omega & 0 & 0 & 0 \\ 0 & 0 & -\mathrm{j}\omega & 0 & 0 \\ 0 & 0 & 0 & -\mathrm{j}5\omega & 0 \\ 0 & 0 & 0 & 0 & \mathrm{j}7\omega \end{bmatrix}. \tag{16}$$

D. Discretization

By defining k as the current multiple of the sample time $T_s (kT_s \equiv t)$, the continuous state space formulation is equivalently discretized by calculating the matrix exponential $e^{\boldsymbol{A}Ts}$ to obtain the discrete system matrix $\boldsymbol{A}_{\mathrm{d}}$ [37]

$$\boldsymbol{x}(k+1) = \underbrace{e^{\boldsymbol{A}(\boldsymbol{s}(k))T_s}}_{\boldsymbol{A_d}(\boldsymbol{s}(k))} \boldsymbol{x}(k) \tag{17}$$

$$\boldsymbol{A_d} = e^{\boldsymbol{A}T_s} = \underbrace{I + \frac{\boldsymbol{A}T_s}{1!}}_{\boldsymbol{A}_{d,ef}} + \underbrace{\frac{(\boldsymbol{A}T_s)^2}{2!} + \frac{(\boldsymbol{A}T_s)^3}{3!} + \cdots}_{\approx 0(\mathrm{approx.error})}. \tag{18}$$

Assuming invariant parameters, the discretization can be numerically done by solving the series expansion (18) for each possible switching state before compiling the control program. Thus, no calculation burden is created during runtime. However, as high sample frequencies $f_s > 20$ kHz are applied, the

$$\boldsymbol{A}_2 = \begin{bmatrix} -\dfrac{R_{fc}}{L_{fc}} & 0 & \dfrac{1}{L_{fc}} & \dfrac{-1}{2L_{fc}}\boldsymbol{T}_{\boldsymbol{\alpha\beta}}\boldsymbol{s} & 0 \\ 0 & -\dfrac{R_{fg}}{L_{fg}} & \dfrac{-1}{L_{fg}} & 0 & 0 \\ \dfrac{R_f R_{fc}}{L_{fc}} - \dfrac{1}{C_f} & \dfrac{1}{C_f} - \dfrac{R_f R_{fg}}{L_{fg}} & -R_f\left(\dfrac{1}{L_{fc}} + \dfrac{1}{L_{fg}}\right) & \dfrac{R_f}{2L_{fc}}\boldsymbol{T}_{\boldsymbol{\alpha\beta}}\boldsymbol{s} & 0 \\ \dfrac{3}{4C_{\mathrm{dc}}}\boldsymbol{s}^T\boldsymbol{T}_{\boldsymbol{\alpha\beta}}^T & 0 & 0 & 0 & \dfrac{-1}{C_{\mathrm{dc}}} \\ 0 & 0 & 0 & 0 & 0 \end{bmatrix}. \tag{12}$$

Euler forward discretization $\boldsymbol{A}_{\mathrm{d,ef}}$ is utilized and the associated approximation error of higher order terms is neglected.

III. Finite Control Set MPC

A. Principle

For FCS-MPC each predicted system state vector $\boldsymbol{x^p}\left(\vec{\boldsymbol{s}}_n\right)$ as a function of feasible inverters switching trajectories $\vec{\boldsymbol{s}}_n = \boldsymbol{s}\left(k\right)|\boldsymbol{s}\left(k+1\right)|\cdots|\boldsymbol{s}(k+n), \vec{\boldsymbol{s}}_n \in \mathcal{S}^n$ is evaluated at the initial sampling instant k along the prediction instants $n \in \{1,\ldots,N^p\}$ until the prediction horizon $N^p \in \mathbb{N}$. Calculation takes place on the basis of the afore mentioned discrete state-space model (14)–(16), which is continued for subsequent prediction instants along N^p, as noted

$$\boldsymbol{x^p}\left(\vec{\boldsymbol{s}}_n\right) = \boldsymbol{A}\left(\boldsymbol{s}\left(k+n\right)\right)\boldsymbol{x}\left(\vec{\boldsymbol{s}}_{n-1}\right) \forall \vec{\boldsymbol{s}}_n \in \mathcal{S}^n. \tag{19}$$

Each prediction instant $\boldsymbol{x^p}\left(\vec{\boldsymbol{s}}_n\right)$ is rated by calculating the partial cost function $g\left(\vec{\boldsymbol{s}}_{n-1}, \boldsymbol{s}\left(n\right)\right)$, cf. (20). This evaluates the predicted system states referred to the desired system state $\boldsymbol{x}^*(n)$ of the reference trajectory $\vec{\boldsymbol{x}}^*$ at sampling instant $k+n$, thus determining the transition cost from state $\boldsymbol{x^p}\left(\vec{\boldsymbol{s}}_{n-1}\right)$ to $\boldsymbol{x^p}\left(\vec{\boldsymbol{s}}_n\right)$. By minimizing the total cost $G\left(\vec{\boldsymbol{s}}\right) \forall \vec{\boldsymbol{s}} \in \mathcal{S}^{N^p}$ (21), the optimal path $\vec{\boldsymbol{s}}^*$ in the prediction tree is selected and the associated switching vector for the next sampling instant $\vec{\boldsymbol{s}}^*(n=1)$ is applied to the system. The control loop is closed by repeating the algorithm each sampling instant (the receding horizon principle) [38]

$$g\left(\vec{\boldsymbol{s}}_{\boldsymbol{n}}\right) = g\left(\vec{\boldsymbol{s}}_{n-1}, \boldsymbol{s}\left(n\right)\right) = f\left[\boldsymbol{x^p}\left(\vec{\boldsymbol{s}}_n\right), \boldsymbol{x}^*(n)\right] \tag{20}$$

$$\min_{\vec{\boldsymbol{s}}}\left\{G\left(\vec{\boldsymbol{s}}\right) = \sum_{n=1}^{Np} g\left(\vec{\boldsymbol{s}}_{n-1}, \boldsymbol{s}(n)\right), \forall \vec{\boldsymbol{s}} \in \mathcal{S}^{Np}\right\} \rightarrow \vec{\boldsymbol{s}}^*. \tag{21}$$

B. Switching Frequency Reduction

It is assumed that the absolute cost function g_i is quadratic and is affected by the weight factor λ_i for current tracking and $n_{\mathrm{sw}}\left(\vec{\boldsymbol{s}}_{n-1}, \vec{\boldsymbol{s}}_n\right)$, which defines the number of commutations from state $\vec{\boldsymbol{s}}_{n-1}$ to $\vec{\boldsymbol{s}}_n$. Adding n_{sw} with a gain λ_{sw}, the cost function punishes trajectories with many switching operations, which leads to a reduced average switching frequency and lower switching losses within the IGBT modules [24], [25], [39]. By appending the reciprocal current prediction horizon $1/n$, earlier commutations are penalized harder than later ones, which defers commutations for a late-switching strategy [26]

$$g(\vec{\boldsymbol{s}}_n) = \underbrace{\lambda_i \cdot \left|\underline{i}^p(\vec{\boldsymbol{s}}_n) - \underline{i}^*(k+n)\right|^2}_{g_i} + \frac{\lambda_{\mathrm{sw}}}{n} \cdot n_{\mathrm{sw}}\left(\vec{\boldsymbol{s}}_{n-1}, \vec{\boldsymbol{s}}_n\right). \tag{22}$$

It is worth mentioning that higher gains λ_{sw} lead to lower switching frequencies and vice versa. However, a bigger weight on switching issues does compromise the current tracking performance and increases current distortion.

C. Practical Implementation Aspects

In a real-time implementation, the execution time of the control algorithm demands the major part of the sample period, leading to a one sampling period system delay between inputs and actuation. In [40], it is shown that the effect of the time delay has a negative impact on the prediction and control performance. This issue is solved with a simple delay compensation scheme by modifying the initial system state vector $\boldsymbol{x}(k)$ to $\boldsymbol{x}(k+1)$ with an early prediction step and the active switching state $\boldsymbol{s}(k)$ at sampling instant *k*.

In [26], several strategies for long-time predictions (multiple samples ahead) with reduced computation complexity are presented. Based on this study, flexible prediction sequences (e.g., {C,E,C,E}) are introduced to FCS-MPC, consisting of control (C) and extension (E) steps and replacing the classic idea of prediction and control horizons. In (C) steps, all possible switching vectors are evaluated, while the (E) steps only extend the preceding switching state to a later point in time. The latter is done by extrapolating the system variables or computing the prediction step (19). To achieve longer prediction steps, it is also possible to use multiple discrete system matrices $\boldsymbol{A_d}(\boldsymbol{T_{prd}}, \boldsymbol{s})$, which are discretized based on lower sampling frequencies $f_{\mathrm{prd}} = 1/T_{\mathrm{prd}} < f_s$. Thus, this method is referred to as downsampling strategy.

For efficient and fast real-time calculation, the used control script is based on a recursive object-oriented programming algorithm. Also redundant zero switching vectors are predicted only once and linked by pointers in the prediction tree. Furthermore, redundancies in the system matrices are analyzed, calculations executed only once and then cached for further uses. If the algorithm execution time still exceeds the sampling period, a reduced switching graph algorithm [41] is used to decrease the calculation burden, considering only switching sequences with one commutation per sample $n_{\mathrm{sw}}\left(\vec{\boldsymbol{s}}_{n-1}, \vec{\boldsymbol{s}}_n\right) = 1$. However, this approach impairs the control performance as the solution space of the optimization problem is restricted.

IV. State Feedback and AD Approaches

A. Control Problem

The goal of grid-connected VSC control is the independent control of active and reactive power supplied to or drawn from the grid. Therefore, the VOC scheme is utilized, which is based on the phase angle of the line voltage u_{PCC} [42]. Since an *LCL* filter is used for grid connection, resonant frequencies are introduced to the plant. In Fig. 2, the associated Bode diagrams of the *LCL* filter are illustrated. Two resonance frequencies f_{res1} and f_{res2} are identified

$$f_{\mathrm{res1}} = \frac{1}{2\pi}\sqrt{\frac{L_{fc}+L_{fg}}{C_f L_{fc} L_{fg}}} \tag{23}$$

$$f_{\mathrm{res2}} = \frac{1}{2\pi}\frac{1}{\sqrt{C_f L_{fg}}}. \tag{24}$$

In [27], *LCL* filter parameter design guidelines applied for PWM-based control approaches are presented. Contrary to those indirect control strategies with fixed average switching frequencies f_{sw}, in FCS-MPC f_{sw} is variable. The average switching frequency of FCS-MPC is difficult to determine in advance since it depends on the specific controller design and the converters operating point. Consequently, the *LCL* filter design task is influenced by the controller properties and vice versa. Also the

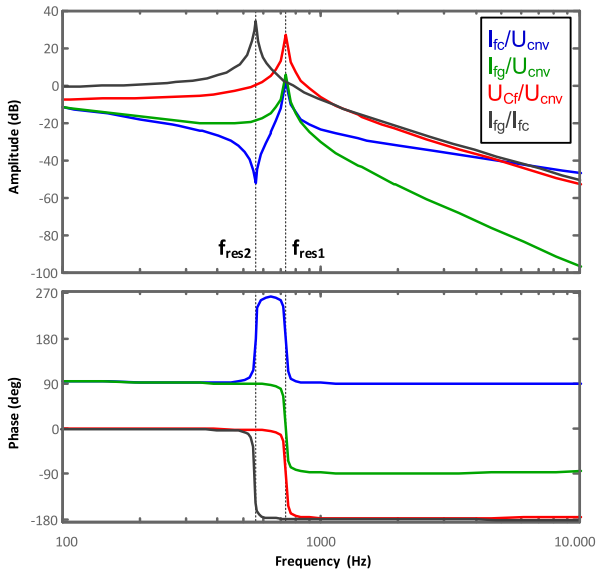

Fig. 2. Bode plot of *LCL* filter transfer functions.

TABLE I
LCL FILTER DESIGN CONSTRAINTS

Symbol	Description	Value (p.u.)
$f_{\mathrm{sw,min}}$	Minimal average switching frequency	30 p.u.
$L_{g,\mathrm{max}}$	Maximal grid inductance	0.0125 p.u.
$f_{\mathrm{res1,min}}$, $f_{\mathrm{res2,min}}$	Minimal resonance frequencies	10 p.u.
$f_{\mathrm{res1,max}}$, $f_{\mathrm{res2,max}}$	Maximal resonance frequencies	15 p.u.
$\lvert L_{fc}+L_{fg}\rvert_{\mathrm{max}}$	Maximal total inductance	0.1 p.u.
$x_{r,\mathrm{max}}$	Maximal reactive power	0.08 p.u.
$\left\lvert \frac{I_{fc}(f_{\mathrm{sw,min}})}{U_{\mathrm{cnv}}(f_{\mathrm{sw,min}})} \right\rvert_{\mathrm{max}}$	Minimal converter-side current damping	−20 dB
$\left\lvert \frac{I_{fg}(f_{\mathrm{sw,min}})}{U_{\mathrm{cnv}}(f_{\mathrm{sw,min}})} \right\rvert_{\mathrm{max}}$	Minimal line-side current damping	−34 dB

resonance frequencies are affected by the present grid impedance which can be modeled as an inductance L_g in series to L_{fg}.

Assuming a maximal grid inductance $L_{g,\mathrm{max}}$ for a maximal offset of the *LCL* filter resonance frequency and a minimal average switching frequency $f_{\mathrm{sw,min}}$, the standard filter design procedures from [27] are adapted in a first step. The considered design constraints are given in Table I with base values from Table IV (see the Appendix). In a second step, the *LCL* filter parameters are validated in simulations and experiments at different operating points while progressively tuning the *LCL* filter for sufficient damping of line current distortion, leading to the *LCL* filter parameters indicated in Table IV (see the Appendix).

B. Converter-Side Current i_{fc} Control (Without Additional AD)

Feedback of the converter-side current i_{fc} is the simplest solution for current tracking as the converter current is highly dynamic and resonances are easy to handle with proper *LCL* filter design, even with small prediction horizons $N^p \leq 2$. A quadratic cost function in stationary $\alpha\beta$ reference frame is used, as shown in (25). For simplification the notations of cost functions are given without commutations penalizing term

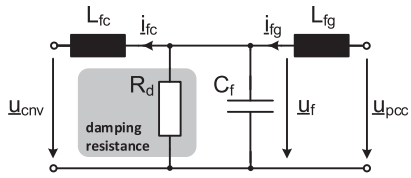

Fig. 3. Single-phase block diagram of damped *LCL* filter by adding parallel (virtual) damping resistance.

and for $N^p = 1$ in the following. The reference values of the converter-side current $\underline{i}_{fc}^{dq*}$ are given by an outer dc-link voltage-control loop and the desired reactive power in *dq* rotating reference frame. The values are then transformed to $\alpha\beta$ stationary-reference-frame-based $\underline{i}_{fc}^{*}(k+n)$ along the predicted horizon $n \in \{1,\ldots,N^p\}$ in each case with the adjusted transformation angle $\theta(k+n)$ according to (26)

$$g = \lambda_i \cdot \left| i_{fc}^{p} - \underline{i}_{fc}^{*} \right|^2 \tag{25}$$

$$\underline{i}_{fc}^{*}(k+n) = \underline{i}_{fc}^{dq*}(k) \cdot \exp\left[-\underbrace{\left(\theta(k) + n \cdot \frac{\omega_0}{f_s} \right) \bmod 2\pi}_{\theta(k+n)} \right]. \tag{26}$$

To compensate for the reactive power consumption of the *LCL* filter, a feed-forward term is added to the converter-side current reference value $^{*}_{fc}$, given as follows:

$$i_{fc}^{q*}(k+n) = i_{fg}^{q}(k+n) - \omega_0 C_f \frac{|u_f(k+n)|^2}{|u_{\mathrm{PCC}}(k+n)|}. \tag{27}$$

One drawback with using the converter-side current i_{fc} as feedback is that the line-side current i_{fg} may be distorted since switching-induced harmonics that appear in the waveforms of i_{fc} are amplified to i_{fg} due to the *LCL* filter resonance f_{res2} (see Section V-E). Despite the system may run in stable operations point, depending on the *LCL* filter setup, often those line-side current distortions do not satisfy the operator's grid code requirements.

C. Converter-Side Current i_{fc} Control With Virtual Resistance AD (VR-AD)

To avoid or mitigate resonant effects in the converter-side current i_{fc} feedback, additional AD networks are applied. Resistances in between the *LCL* filter components help to dampen the oscillations, as shown in Fig. 3. However, adding resistances to the filter (passive damping) induces additional ohmic losses. This is contrary to the ultimate goal of achieving high-efficiency power conversion systems.

A well-known approach to mitigate these losses is to use a virtual resistance (VR)-based AD concept by using additional feedback of the filter voltage u_f [30], [31], [43]. This method simulates a damping resistance R_{dp} by injecting an additional converter-side current component. While different realizations of the damping resistance (parallel or in series to C_f, L_{fc}, or L_{fg}) are possible, the parallel damping resistance approach is straightforward as no differentiator is necessary [31]. Here, due

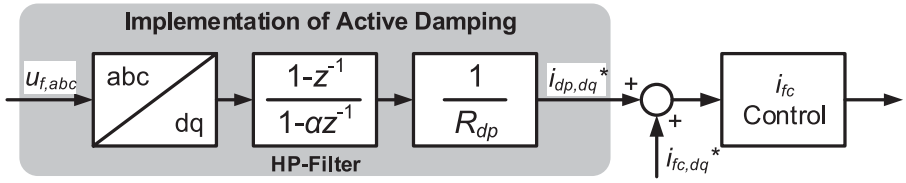

Fig. 4. Block diagram of VR-AD for u_f and i_{fc} feedback.

to a minimal calculation burden the virtual damping resistance R_{dp} in parallel to the filter capacitance C_f is applied, realized by injecting a i_{fc} component in phase to $\underline{u}_f$. Additionally, to avoid power flow disturbances, the fundamental voltage waveform is extracted from $\underline{u}_f$. To achieve this, the fundamental is transformed into a dc signal by *dq* transformation and then removed by applying a simple first-order infinite impulse response (IIR) high-pass filter. The filtered signal then is divided by the desired damping resistance and added to the current reference. The block diagram of this VR-AD approach is shown in Fig. 4.

Problems may occur as soon as the line voltage is distorted by harmonics, which cannot be dampened by VR-AD. In this case, those harmonics are continuously fed back to the current reference leading to increased distortion of the line-side current waveforms. The harmonics of order λ in the line-side current $I_{fg}(\lambda f_0)$ (here, f_0 denotes the fundamental frequency) will propagate in all settings if the voltages $U_f(\lambda f_0)$ and $U_{\mathrm{PCC}}(\lambda f_0)$ differ in amplitude and/or phase.

D. Converter-Side Current i_{fc} and Filter Voltage u_f Multivariable Control

To reduce the aforementioned negative effects of line-side current distortion, it is desirable to control the filter voltage u_f in a way that $U_f(\lambda f_0) = U_{\mathrm{PCC}}(\lambda f_0)$ is achieved. FCS-MPC enables multivariable control, which controls the filter voltage u_f on a reference trajectory in addition to the standard converter-side current i_{fc}. Treating the current reference $\underline{i}^*_{fg}$ as steady state at fundamental angular frequency ω_0, the filter-voltage reference $\underline{u}^*_f$ is calculated using (28) through the R_{fg} and L_{fg} branch. At this point, the extended system model (14)–(16) is utilized. The extended system model enables the consideration of harmonics both in the predictions and the reference trajectory

$$\begin{aligned}\underline{u}^*_f(k+n) \;=\; & \underline{u}_{\mathrm{PCC},1p}(k)e^{\mathrm{j}\frac{\omega_0}{2\pi}n} + \underline{u}_{\mathrm{PCC},1n}(k)e^{-\mathrm{j}\frac{\omega_0}{2\pi}n} \\ & + \underline{u}_{\mathrm{PCC},5n}(k)e^{-\mathrm{j}\frac{5\omega_0}{2\pi}n} + {}_{\mathrm{PCC},7p}(k)e^{\mathrm{j}\frac{7\omega_0}{2\pi}n} \\ & - (R_{fg} + \mathrm{j}\omega_0 L_{fg})\,\underline{i}^{dq*}_{fg}(k)e^{-\theta(n)}. \end{aligned} \tag{28}$$

The related cost function is given in (29). Because of different magnitudes and operating point dependencies, the cost function is normalized by dividing the square of the absolute measured values. The current normalization is recommended based on the filtered line-side current i_{fg} as these waveforms are less distorted by switching harmonics. Further, attention must be paid to the choice of the weighting factors λ_i and λ_u in the cost function because current tracking should be prioritized

$$g = \frac{\lambda_i}{\left|\underline{i}_{fg}\right|^2}\left|\underline{i}^p_{fc} - \underline{i}^*_{fc}\right|^2 + \frac{\lambda_u}{\left|\underline{u}_f\right|^2}\left|\underline{u}^p_f - \underline{u}^*_f\right|^2. \tag{29}$$

As two of three states of the *LCL* filter are controlled, the uncontrolled resonant energy oscillation between the inductances and the capacitance is effectively avoided. On the downside, the cost function (29) is more complex compared to single-variable control in terms of calculation burden and control parameter design. Model inaccuracies and the steady-state assumption make this multivariable approach prone to current deviations from the set point, as shown in the measurement study in Section V.

E. Line-Side Current i_{fg} Control (Without AD)

The straightforward approach of controlling the power at PCC is using a direct line-side current i_{fg} feedback as no reactive power compensation is necessary. The simple cost function (30) proves to be beneficial as well. However, this approach requires control and prediction horizons $N^p > 1$ due to the fact that the predicted value of i_{fg} cannot be directly manipulated by $\boldsymbol{S}$ when utilizing the Euler forward discretization

$$g = \lambda_i \cdot \left|\underline{i}^p_{fg} - \underline{i}^*_{fg}\right|^2. \tag{30}$$

Due to the third-order filter effect reducing high frequency switching harmonics, much fewer switching operations are necessary to track sinusoidal fundamental reference trajectories in the line-side currents i_{fg} instead of in the converter currents i_{fc}. However, studying the long switching patterns reveals that the converter current spectrum is shifted towards the *LCL* filters Eigen frequencies, exciting the resonance to unstable operation. Considering that the system model represents all relevant system dynamics, the model predictive controller should anticipate switching trajectories which excite resonances and automatically exclude them as they cause high set point deviations and huge costs. While this theory may be valid for infinite prediction horizons, the FCS-MPC algorithm with small horizons cannot properly evaluate this effect because of the nonnegligible filter delay. Increasing the prediction horizon is bounded to limits implied by the exponential growing calculation burden. Nevertheless, it is possible to design controllers on standard hardware for long-time predictions with reduced computation complexity, such as by flexible prediction sequences with downsampling strategies based on a highly efficient algorithm. These measures, which are described in Section III-C, ensure the system's stability.

F. Line-Side Current i_{fg} and Filter Voltage u_f Multivariable Control

Similar to the methodology presented in Section IV-D, it is possible to achieve adequate damping of the system by controlling i_{fg} and u_f. The associated cost function is shown as

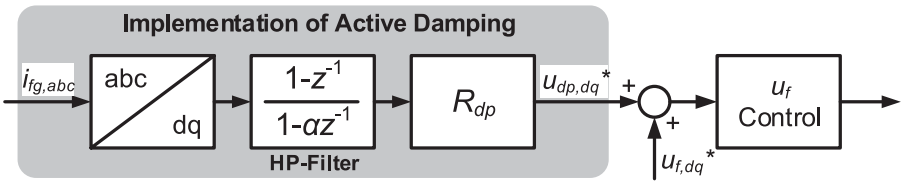

Fig. 5. Block diagram of virtual resistance AD for i_{fg} and u_f feedback.

follows:

$$g = \frac{\lambda_i}{\left|\underline{i}_{fg}\right|^2}\left|\underline{i}_{fg}^{p} - \underline{i}_{fg}^{*}\right|^2 + \frac{\lambda_u}{\left|\underline{u}_f\right|^2}\left|\underline{u}_f^{p} - \underline{u}_f^{*}\right|^2. \qquad (31)$$

Additionally, VR-AD approaches similar to Section IV-C can now be implemented. However, in this case, the filtered line current i_{fg} is added to the filter voltage reference u_f^* as u_f control is more dynamic than i_{fg} control. The resultant control block diagram is shown in Fig. 5.

As previously described, this control strategy is highlighted by a more complex cost function, which is unfavorable in terms of calculation burden and controller design. The tradeoff between those two feedback variables translates into a control performance, which may be hard to anticipate depending on the operating point.

TABLE II
CONTROL PARAMETERS

Control variable(s)	(a) i_{fc}	(b) i_{fc} and u_f	(c) i_{fg}	(d) i_{fg} and u_f
Control sequence	{C,C}	{C,C}	{C,E,C,E}	{C,E,C,E}
Sampling frequency f_s	22 kHz	22 kHz	22 kHz	22 kHz
{E} prediction step T_{prd}	–	–	$2\,T_s$	$2\,T_s$
Reduced switching graph	No	Yes	Yes	Yes
Prediction horizon h	$2\,T_s$	$2\,T_s$	$6\,T_s$	$6\,T_s$
Weighting factor λ_i	3	3	10	10
Weighting factor λ_u	–	10	–	10
Weighting factor λ_{sw}	0.02	0.02	0.02	0.02
Normalization of λ_i	$\lvert i_{fc}(k)\rvert^2$	$\lvert i_{fc}(k)\rvert^2$	$\lvert i_{fg}(k)\rvert^2$	$\lvert i_{fg}(k)\rvert^2$
Normalization of λ_u	$2/3\,U_{\mathrm{PCC}}^2$	$2/3\,U_{\mathrm{PCC}}^2$	$2/3\,U_{\mathrm{PCC}}^2$	$2/3\,U_{\mathrm{PCC}}^2$
AD HP-filter factor α	0.98	–	–	0.98
AD virtual resistance R_{dp}	25 Ω	–	–	1 Ω

V. SIMULATION AND MEASUREMENT STUDY

A measurement study is carried out to examine FCS-MPC control strategies with the presented feedback approaches under laboratory conditions. The required control parameters are determined in advance in a MATLAB/Simulink simulation environment with additional PLECS toolbox. For a comparison, the best feasible control parameter setting for each control strategy has been experimentally determined in advance. The converter-side current feedback strategies perform better without (E) sequences due to the unfiltered and highly dynamic character of i_{fc}. In those cases, long prediction steps lead to unfavorable switching trajectories as switching within the extension step might be optimal. On the other hand, the implementation of (E) sequences is strongly advisable for line-side current feedback strategies due to the filtered and less dynamic characteristic of i_{fg}. Considering the response characteristics of the third-order *LCL* filter, longer prediction horizons are necessary to overcome the filter delay and to properly evaluate the future system states induced by the switching behavior (see Section IV-E). Thus, a feasible long-time prediction strategy with (E) steps improves the control performance and stability. As a result of computing restrictions, the reduced switching graph [41] has to be utilized for all methods except pure converter-side current i_{fc} feedback. Table II summarizes the selected control parameters for the different AD approaches.

A. Test-Bench Description and Measurement Methodology

A 22-kW laboratory system is used to validate the proposed control concepts. The system is composed of a frequency converter with two-level VSI in back-to-back configuration. To achieve an adjustable dc-load current one VSI is connected to a three-phase, grid-fed galvanic isolated step-up transformer, whereas the other VSI (here: the device under test, DUT) is directly connected to the ac mains. By raising the transformer-output voltage above the dc-link voltage u_{dc}, a load current through the IGBTs freewheeling diodes is established. An *LCL* filter is used to connect the DUT VSI to the mains. The control algorithms are implemented on a dSpace DS1006 board with custom-written digital waveform output (DWO) codes for IGBT pulse signal generation as well as for synchronized sampling and switching procedures. The general system parameters are summarized in Table IV in the Appendix. All presented measurements are performed on the same experimental setup without changing the system parameters.

B. Dynamic Control Performance

For examining the control dynamics, a reference-value step of reactive current $i_{fg}^{q*} = 0 \rightarrow 15\mathrm{A}$ is carried out while the active current reference remains constant $i_{fg}^{d*} = 20\mathrm{A}$. To achieve comparable operating points, the reference-value step is synchronously triggered when the phase jump of the grid-voltage phase angle $\theta = 2\pi \rightarrow 0$ is identified.

As shown by the measurement results in Fig. 6, high dynamic current tracking is achieved for all four methods. In case of converter-side current feedback [see Fig. 6(a) and (b)], the i_{fc} reference is adjusted and achieved within three to four sample periods. However, the line-side current follows up with a rise time $t_r \approx 0.7$ ms and about 50% percentage overshoot (PO). Additional u_f feedback reveals a negligible impact in terms of dynamics in the present control setup, even though i_{fc} and u_f feedback is carried out with the reduced switching graph [41].

In case of line-side current feedback, the i_{fg} reference value is adjusted in $t_r \approx 0.5$ ms and with less overshoot of $PO \approx 13\%$. On the downside, the filter system resonance f_{res2} seems to be excited in the d-current by long-pulse switching patterns, as shown in Fig. 6(c). Nevertheless, the resonance is proper damped afterward and the system remains stable. Longer

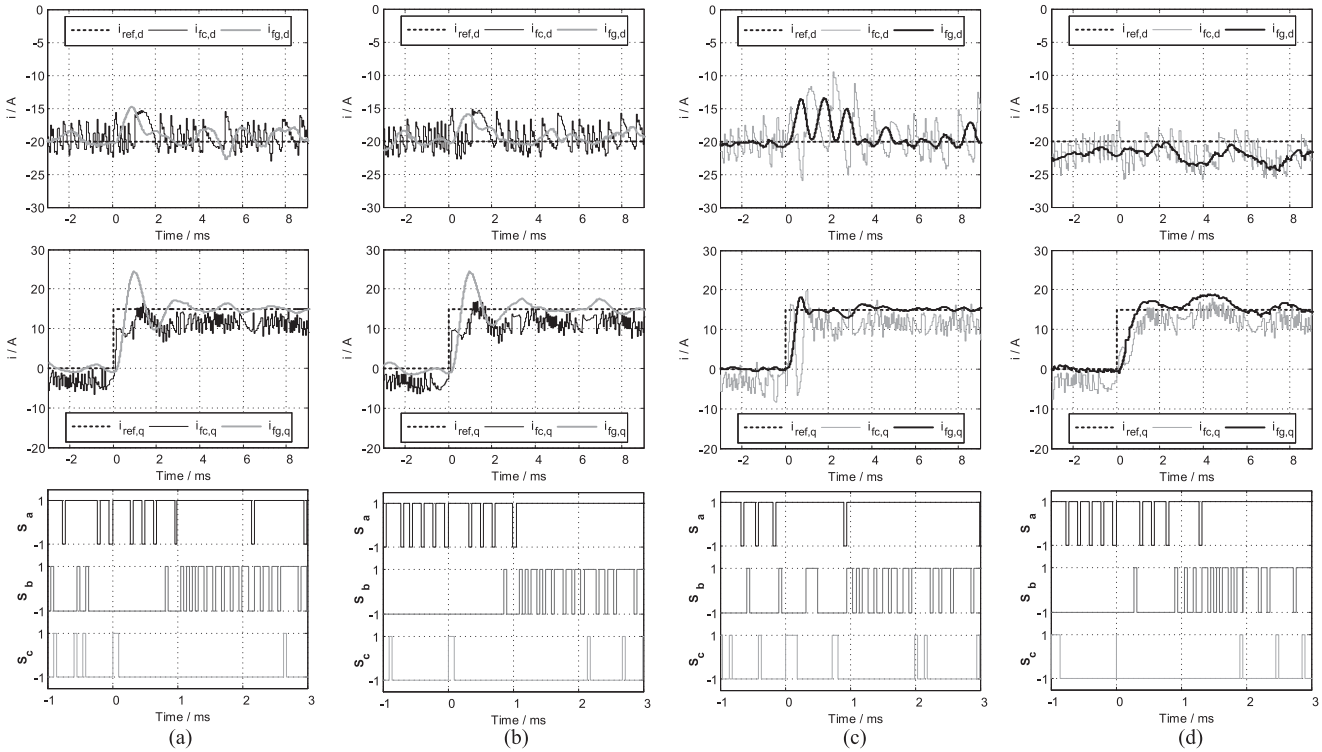

Fig. 6. Measured step responses in *dq* coordinates and related switching patterns (zoom) for different AD strategies of: (a) converter-side current i_{fc} feedback, (b) converter-side current i_{fc} and filter voltage u_f feedback, (c) line-side current i_{fg} feedback, and (d) line-side current i_{fg} and filter-voltage u_f feedback.

TABLE III
MEASURED DYNAMIC AND STEADY-STATE CONTROL PERFORMANCE FOR DIFFERENT AD CONCEPTS

Control Variable(s)	(a) i_{fc}	(b) i_{fc} and u_f	(c) i_{fg}	(d) i_{fg} and u_f
t_r (i_{fg})	0.7 ms	0.7 ms	0.5 ms	1.0 ms
PO (i_{fg})	∼50%	∼50%	∼13%	∼10%
THD_{40} (i_{fg})	4.7%	3.9%	2.1%	5.1%

prediction horizons tend to avoid those resonance problems and stabilizing the system during transients. It is worth mentioning that the i_{fc} current ripple is bigger due to the decreased average switching frequency necessary for i_{fg} tracking. Adding u_f feedback to the cost function reveals a major impact on the dynamics of i_{fg} in this case, doubling the rise time to $t_r \approx 1.0$ ms. As it can be seen from Fig. 6(d), a steady-state deviation in the *d*-current of approximately 2.5 A is caused by the second control variable. However, the AD approach successfully avoids resonance excitation during the transients. The dynamic control performances of the presented approaches are summarized in Table III.

In Fig. 7, the corresponding simulation results of the measured step responses presented in Fig. 6 are illustrated. The simulations have been carried out utilizing the same parameter and control settings for each feedback strategy as discussed before. Besides a slightly higher current ripple observed in simulation, these results reveal a high degree of conformity compared to the presented measurement results. The higher current ripple is traced back to not modeled blanking-time effects of the underlying simulation model.

C. Steady-State Control Performance

For steady-state performance, the system is examined with both constant $i_{fg}^{d*} = 20\text{A}$ and $i_{fg}^{q*} = 15\text{A}$ current references. The resulting three-phase current waveforms are presented in Fig. 8. Despite AD, the line-side current is still distorted by harmonics that are mainly induced by the resonant pole at f_{res1} and the distinctive fifth and seventh harmonics in the filter voltage [see Fig. 8 (a)]. Those are fed back to the current reference by the AD approach. By adding u_f control to the cost function, u_{PCC} disturbance rejection is improved and the line-side current i_{fg} has less distortion [see Fig. 8(b)]. The best result is achieved with i_{fg} feedback only, as shown in Fig. 8(c), and it is worth mentioning that this almost sinusoidal current is achieved with the lowest average switching frequency of all methods $f_{\text{sw}} \approx 1.6$ kHz at the same time. By contrast, additional u_f feedback causes a significant higher distortion [see Fig. 8(d)]. This characteristics can be shifted between (c) and (d) by modifying the u_f tracking weight in the cost function. However, with smaller weight factors, it is more likely to excite the resonances during transients. The steady-state results are quantified and aggregated by the total harmonic distortion of the line-side current i_{fg} in Table III.

D. Switching Frequency Reduction Performance

For comparing the switching frequencies, the converter is operated at steady state with $i_{fg}^{d*} = 35\text{A}$ and $i_{fg}^{q*} = 0\text{A}$ and the switching cost weight factor K_{sw} is varied in the interval of $K_{\text{sw}} \in \{0.00, 0.02, \ldots, 0.18, 0.20\}$. The switching frequency is plotted against the total harmonic distortion of the line-side current i_{fg} in Fig. 9.

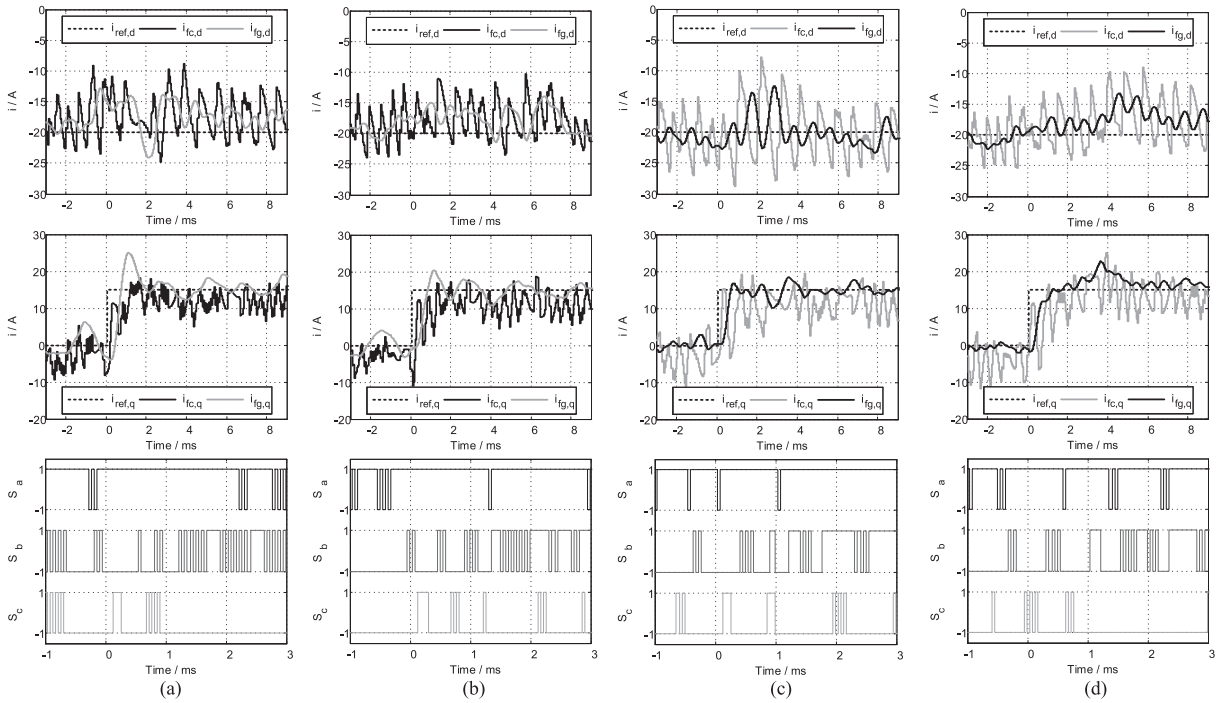

Fig. 7. Simulated step responses in *dq* coordinates and related switching patterns (zoom) for different AD strategies of: (a) converter-side current i_{fc} feedback, (b) converter-side current i_{fc} and filter voltage u_f feedback, (c) line-side current i_{fg} feedback, and (d) line-side current i_{fg} and filter voltage u_f feedback.

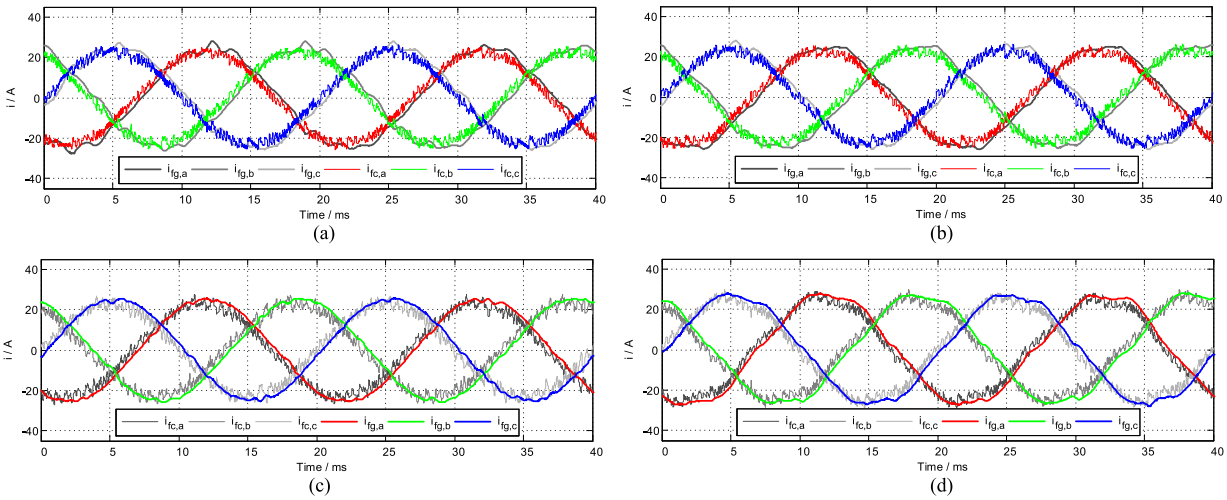

Fig. 8. Measured *abc* current waveforms in steady-state conditions for different AD strategies of: (a) converter-side current i_{fc} feedback, (b) converter-side current i_{fc} and filter voltage u_f feedback, (c) line-side current i_{fg} feedback, and (d) line-side current i_{fg} and filter voltage u_f feedback.

As can be seen, multivariable control with i_{fc} and u_f feedback is beating standard control with i_{fc} feedback with less current distortion for the same switching frequency in the evaluated operating points. However, control with i_{fg} feedback outperforms all other methods. In contrast, additional u_f feedback impairs the result. Even though the distortion is similar to i_{fc} feedback in this case. Also the same weight factor K_{sw} reveals less influence on the switching frequency than with the other feedback approaches.

E. VR-AD Performance

The effect of virtual resistance AD is illustrated in Fig. 10. As soon as AD is turned off, the resonance from the resonant pole in the current transfer function at f_{res1} is excited. Consequently, the line-side current i_{fg} gets significantly distorted.

When looking at the three-phase average current spectrum in Fig. 11, it is obvious that the proposed AD concept is highly effective at damping the resonance oscillations f_{res1} from 15% to 2% of the fundamental current amplitude. Thus, in this case, AD is mandatory for satisfying grid-code compliance for power quality.

F. Comparison of Different Control Approaches

For the case of networks, which are badly affected by harmonics, the i_{fc} and u_f feedback approach (b) performs better than i_{fc} feedback (a). While the transient behavior is comparable, the line-side current distortion is improved by

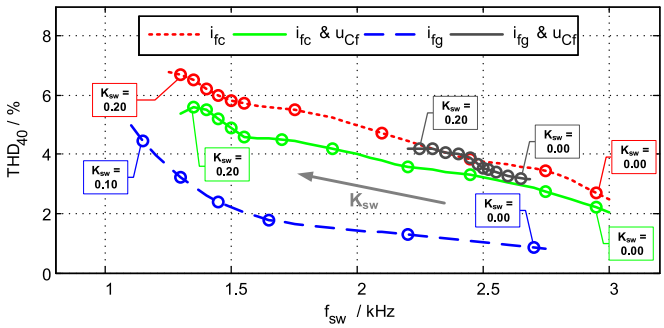

Fig. 9. Measured total harmonic current distortion (THD) versus average switching frequency f_{sw} in steady-state conditions for different AD feedback approaches.

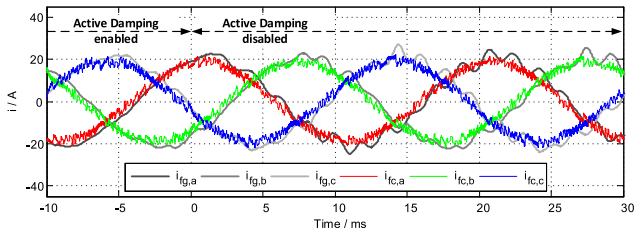

Fig. 10. Measured *abc* current waveforms with and without AD.

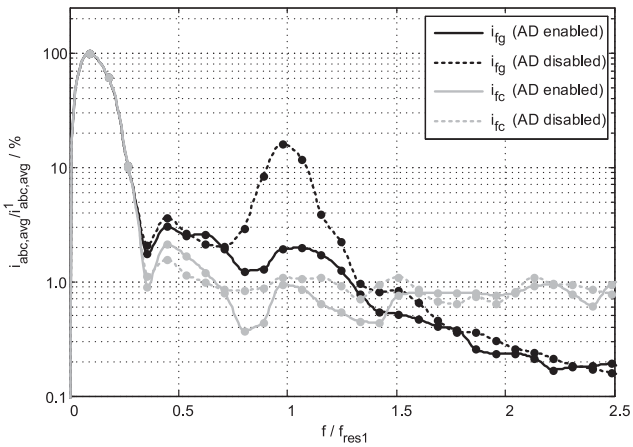

Fig. 11. Three-phase average (normalized) current spectrum with AD enabled or disabled (i_{fc} feedback).

manipulating u_f to follow a suitable reference trajectory (see Section IV-D).

For the case of reducing switching losses and/or steady-state line-side current distortion, the i_{fg} feedback approach (c) is superior to the other control strategies (see Fig. 9). Furthermore, the transient response of i_{fg} is the most dynamic in comparison. Nevertheless, resonance excitation and stability may be critical with feasible prediction horizons. Adding u_f feedback, the i_{fg} and u_f multivariable control (d) improves the suppression of resonances but impairs both the dynamic and steady-state control performance compared to i_{fg} feedback (c).

In terms of complexity, the multivariable control strategies (b) and (d) are the most sophisticated approaches as they demand more calculation power to calculate the additional cost function section and the u_f set point trajectory. Moreover, due to the added control parameters, tuning the controller becomes more complex. On the contrary, the single feedback strategies (a) and (c) are simpler to tune and require less calculation burden. However, line-side current control (c) demands long prediction horizons, which makes it significantly more challenging for control hardware than (a).

VI. Discussion

The control performance of the presented FCS-MPC algorithm for *LCL* filters is presented by practical analysis. However, there are some limitations and open issues of the proposed control approaches that are discussed in this section.

First, it is assumed that the modeled system parameters match the actual physical setup. As the FCS-MPC is based on a system model, depending on the controlled system, feedback variables, and control parameters the FCS-MPC algorithm is sensitive to parameter variations. While stability was no issue with i_{fc} feedback strategies (a and b) in the analyzed setup with parameter variations up to 50%, increasing model parameter deviations can cause stability problems with i_{fg} feedback (c and d). This is the result of adulterated predictions of the modeled system transient response which impedes the controller's ability to anticipate resonance oscillations. Also the stability margin at i_{fg} feedback is smaller due to the challenging filter delay. Besides, in all feedback variants (a–d) model parameters mismatches increase the distortion of currents i_{fc} and i_{fg}. Also may model mismatches lead to a steady-state error for the multivariable control strategies (b) and (c) as the calculated reference trajectory u_f^* is biased.

Second, as sampling and switching take place at the beginning of a control period in this FCS-MPC setup, measured values may not correspond to the mean value of currents and voltages. As a result, the adjusted reference value may differ from the mean system value, leading to a steady-state error. In [46] and [47], this effect is studied and approaches to overcome this issue are proposed. Moreover, as this error is more relevant for lower sampling frequencies, it is neglected for the examined setup with $f_s = 20$ kHz.

Third, the measurement study is carried out on a laboratory system with an *LCL* filter setup, which was determined with assumptions and constraints of *LCL* filter parameter design guidelines for PWM-based controllers presented in [27] (see Section IV-A). As the *LCL* filter design task is influenced by the controller properties and vice versa, special attention was paid to identify a suitable filter setup in advance. However, a deeper insight how to design *LCL* filters for FCS-MPC applications is highly recommended for future research activities.

VII. Conclusion

In this paper, it is shown that FCS-MPC is able to handle complex control systems like grid-connected converters with *LCL* filters. In this case, resonance issues are addressed by AD approaches like virtual-resistance damping or multivariable control. This is implemented with adjusted cost functions and suitable reference trajectories. Also, inherent model-based AD proved to be possible with long prediction horizons, which is realized for online calculation with advanced optimization techniques. Besides converter-side current feedback, this paper presents and compares three new feedback approaches,

including multivariable control and direct line current control based on FCS-MPC.

As the measurements on the 22 kW laboratory test-bench reveal, all methods present good control performances, satisfying the grid code compliance with low current distortion and featuring low switching frequencies at the same time. The common converter-side current control approach is improved with additional u_f feedback, especially when networks are badly affected with harmonics. Furthermore, the introduced line-side current control strategy with long prediction horizons was revealed to be the most promising solution for reducing switching losses and/or steady-state line-side current distortion. Here, the only potential limitation is calculation power on available control hardware. As smaller prediction horizons are acceptable, converter-side current control is easier to implement than i_{fg} feedback strategies and is also very robust against resonance excitation due to the virtual resistance AD.

The presented FCS-MPC feedback strategies for *LCL*-filter-equipped power converter systems have the potential to be a serious alternative to classical PWM-based control schemes for high-power high-efficiency VSC applications, offering great control performance and reduced switching losses.

APPENDIX

See Table IV.

TABLE IV
MEASUREMENT SYSTEM PARAMETERS

Symbol	Description	Value (per unit)
u_{PCC}	Line-to-line voltage (rms)	400 V (1.0)
I_n	Rated converter current (rms)	32 A (1.0)
ω_0	Angular line frequency	2π 50 Hz (1.0)
L_g	Grid inductance (measured)	80 μH (0.002)
R_g	Grid resistance (measured)	120 mΩ (0.01)
C_{dc}	DC-link capacitance	2200 μF (8.6)
U_{dc}	DC-link voltage (controlled)	650 V (1.6)
L_{fc}	Converter-side filter inductance	3.5 mH (0.09)
R_{fc}	Converter-side filter resistance	210 mΩ (0.02)
L_{fg}	Line-side filter inductance	2.5 mH (0.06)
R_{fg}	Line-side filter resistance	150 mΩ (0.01)
C_f	Filter capacitance	32.4 μF (0.13)
R_f	ESR of filter capacitance	40 mΩ (0.003)
f_{res1}	First filter resonance frequency	726 Hz (14.5)
f_{res2}	Second filter resonance frequency	550 Hz (11.0)

REFERENCES

[1] J. D. V. Wyk and F. C. Lee, "On a future for power electronics," *IEEE Trans. Emerg. Sel. Topics Power Electron.*, vol. 1, no. 2, pp. 59–72, Jun. 2013.

[2] REN21 Renewable Energy Policy Network for the 21st Century, "*Renewables global status report 2014,*" Paris, (2014). [Online] Available: http://www.ren21.net/Portals/0/documents/Resources/GSR/2014/GSR2014_full%20report_low%20res.pdf

[3] S. E. Beid and S. Doubabi, "DSP-based implementation of fuzzy output tracking control for a boost converter," *IEEE Trans. Ind. Electron.*, vol. 61, no. 1, pp. 196–209, Jan. 2014.

[4] R. Khanna, Q. Zhang; W. E. Stanchina, G. F. Reed, and Z.-H. Mao, "Maximum power point tracking using model reference adaptive control," *IEEE Trans. Power Electron.*, vol. 29, no. 3, pp. 1490–1499, Mar. 2014.

[5] O. Barambones and P. Alkorta, "Position control of the induction motor using an adaptive sliding-mode controller and observers," *IEEE Trans. Ind. Electron.*, vol. 61, no. 12, pp. 6556–6565, Dec. 2014.

[6] J. Rodriguez, M. P. Kazmierkowski, J. R. Espinoza, P. Zanchetta, H. Abu-Rub, H. A. Young, and C. A. Rojas, "State of the art of finite control set model predictive control in power electronics," *IEEE Trans. Ind. Informat.*, vol. 9, no. 2, pp. 1003–1016, May 2013.

[7] T. Geyer, "Model predictive direct torque control: Derivation and analysis of the state-feedback control law," *IEEE Trans. Ind. Appl.*, vol. 49, no. 5, pp. 2146–2157, Sep.–Oct. 2013.

[8] J. Scoltock, T. Geyer, and U. K. Madawala, "Model predictive direct power control for grid-connected neutral-point-clamped converters," *IEEE Trans. Ind. Electron.*, vol. 62, no. 9, pp. 5319–5328, Sept. 2015.

[9] N. Hoffmann, M. Andresen, F. W. Fuchs, L. Asiminoaei, and P. B. Thøgersen, "Variable sampling time finite control-set model predictive current control for voltage source inverters," in *Proc. 2012 IEEE Energy Convers. Congr. Expo.*, pp. 2215–2222.

[10] T. Geyer and D. E. Quevedo, "Multistep finite control set model predictive control for power electronics," *IEEE Trans. Power Electron.*, vol. 29, no. 12, pp. 6836–6846, Dec. 2014.

[11] J. Hu, J. Zhu, and D. G. Dorrell, "Model predictive control of grid-connected inverters for PV systems with flexible power regulation and switching frequency reduction," *IEEE Trans. Ind. Appl.*, vol. 51, no. 1, pp. 587–594, Jan.–Feb. 2015.

[12] T. J. Vyncke, S. Thielemans, and J. A. Melkebeek, "Finite-set model-based predictive control for flying-capacitor converters: Cost function design and efficient FPGA implementation," *IEEE Trans. Ind. Informat.*, vol. 9, no. 2, pp. 1113–1121, May 2013.

[13] V. Yaramasu, B. Wu, and J. Chen, "Model-Predictive control of grid-tied four-level diode-clamped inverters for high-power wind energy conversion systems," *IEEE Trans. Power Electron.*, vol. 29, no. 6, pp. 2861–2873, Jun. 2014.

[14] E. Fuentes, D. Kalise, J. Rodriguez, and R. M. Kennel, "Cascade-Free predictive speed control for electrical drives," *IEEE Trans. Ind. Electron.*, vol. 61, no. 5, pp. 2176–2184, May 2014.

[15] D.-K. Choi and K.-B. Lee, "Dynamic performance improvement of AC/DC converter using model predictive direct power control with finite control set," *IEEE Trans. Ind. Electron.*, vol. 62, no. 2, pp. 757–767, Feb. 2015.

[16] R. P. Aguilera, P. Lezana, and D. E. Quevedo, "Finite-control-set model predictive control with improved steady-state performance," *IEEE Trans. Ind. Informat.*, vol. 9, no. 2, pp. 658–667, May 2013.

[17] R. P. Aguilera and D. E. Quevedo, "Predictive control of power converters: Designs with guaranteed performance," *IEEE Trans. Ind. Informat.*, vol. 11, no. 1, pp. 53–63, Feb. 2015.

[18] J. Scoltock, T. Geyer, and U. K. Madawala, "Model predictive direct power control for grid-connected NPC converters," *IEEE Trans. Ind. Electron.*, vol. 62, no. 9, pp. 5319–5328, Sept. 2015.

[19] S. Kwak and J.-C. Park, "Model-Predictive direct power control with vector preselection technique for highly efficient active rectifiers," *IEEE Trans. Ind. Informat.*, vol. 11, no. 1, pp. 44–52, Feb. 2015.

[20] T. Geyer and D. E. Quevedo, "Performance of multistep finite control set model predictive control for power electronics," *IEEE Trans. Power Electron.*, vol. 30, no. 3, pp. 1633–1644, Mar. 2015.

[21] J. R. Fischer, S. A. Gonzalez, M. A. Herran, M. G. Judewicz, and D. O. Carrica, "Calculation-delay tolerant predictive current controller for three-phase inverters," *IEEE. Trans. Ind. Informat.*, vol. 10, no. 1, pp. 233–242, Feb. 2014.

[22] M. P. Kazmierkowski and L. Malesani, "Current control techniques for three-phase voltage-source PWM converters: A survey," *IEEE Trans. Ind. Electron.*, vol. 45, no. 5, pp. 691–703, Oct. 1998.

[23] X. Lie, Z. Dawei, and Y. Liangzhong, "Direct power control of grid connected voltage source converters," in *Proc. 2007 IEEE Power Eng. Soc. General Meeting*, pp. 1–6.

[24] C. Xia, T. Liu, T. Shi, and Z. Song, "A simplified finite-control-set model-predictive control for power converters," *IEEE Trans. Ind. Informat.*, vol. 10, no. 2, pp. 991–1002, May 2014.

[25] M. Preindl and S. Bolognani, "Model predictive direct torque control with finite control set for PMSM drive systems, Part 1: Maximum torque per ampere operation," *IEEE Trans. Ind. Informat.*, vol. 9, no. 4, pp. 1912–1921, Nov. 2013.

[26] T. Geyer, "Low complexity model predictive control in power electronics and power systems," PhD dissertation, Ewiss Federal Institute of Technology Zurich (ETH), Zürich, Switzerland, 2005.

[27] A. Reznik, M. G. Simoes, A. Al-Durra, and S. M. Muyeen, "*LCL* filter design and performance analysis for grid-interconnected systems," *IEEE Trans. Ind. Appl.*, vol. 50, no. 2, pp. 1225–1232, Mar.–Apr. 2014.

[28] B. Hoff and W. Sulkowski, "Grid-connected VSI with LCL filter—Models and comparison," *IEEE Trans. Ind. Appl.*, vol. 50, no. 3, pp. 1974–1981, May–Jun. 2014.

[29] A. A. Rockhill, M. Liserre, R. Teodorescu, and P. Rodriguez, "Grid-filter design for a multimegawatt medium-voltage voltage-source inverter," *IEEE Trans. Ind. Electron.*, vol. 58, no. 4, pp. 1205–1217, Apr. 2011.
[30] J. Scoltock, T. Geyer, and U. Madawala, "Model predictive direct current control for a grid-connected converter: LCL filter versus l-filter," in *Proc. 2013 IEEE Int. Conf. Ind. Technol.*, pp. 576–581.
[31] J. Scoltock, T. Geyer, and U. Madawala, "Model predictive direct power control for a grid-connected converter with an LCL filter," in *Proc. 2013 IEEE Int. Conf. Ind. Technol.*, pp. 588–593.
[32] J. Scoltock, T. Geyer, and U. K. Madawala, "A model predictive direct current control strategy with predictive references for MV grid-connected converters with LCL filters," *IEEE Trans. Power Electron.*, vol. 30, no. 10, pp. 5926–5937, Oct. 2015.
[33] A. B. Baggini, *Handbook of Power Quality*. Chichester, U.K./Hoboken, NJ, USA: Wiley, 2008.
[34] N. Hoffmann, M. Hempel, M. C. Harke, and F. W. Fuchs, "Observer-based grid voltage disturbance rejection for grid connected voltage source PWM converters with line side LCL filters," in *Proc. 2012 IEEE Energy Convers. Congr. Expo.*, pp. 69–76.
[35] G. J. Wakileh, *Power Systems Harmonics: Fundamentals, Analysis, and Filter Design*. Berlin, Germany/New York, NY, USA: Springer, 2001.
[36] P. Rodríguez, A. Luna, I. Candela, R. Mujal, R. Teodorescu, and F. Blaabjerg, "Multiresonant frequency-locked loop for grid synchronization of power converters under distorted grid conditions," *IEEE Trans. Ind. Electron*, vol. 58, no. 1, pp. 127–138, Jan. 2011.
[37] W. S. Levine, *The Control Handbook*. Boca Raton, FL, USA/New York, NY, USA: CRC Press/IEEE Press, 1996.
[38] L. Grüne and J. Pannek, *Nonlinear Model Predictive Control: Theory and Algorithms*. London, U.K./New York, NY, USA: Springer, 2011.
[39] U. Ammann, R. Vargas, and J. R. Stielow, "Investigation of the average switching frequency of direct model predictive control converters," in *Proc. 2010 IEEE Conf. Ind. Technol.*, pp. 1800–1807.
[40] P. Cortes, J. Rodriguez, C. Silva, and A. Flores, "Delay compensation in model predictive current control of a three-phase inverter," *IEEE Trans. Ind. Electron*, vol. 59, no. 2, pp. 1323–1325, Feb. 2012.
[41] M. Preindl and E. Schaltz, "Load torque compensator for model predictive direct current control in high power PMSM drive systems," in *Proc. 2010 IEEE Int. Symp. Ind. Electron.*, pp. 1347–1352.
[42] M. P. Kazmierkowski, R. Krishnan, and F. Blaabjerg, *Control in Power Electronics: Selected Problems*. Amsterdam, The Netherlands: Academic, 2002.
[43] M. Rivera, P. Correa, J. Rodriguez, I. Lizama, J. Espinoza, and C. Rojas, "Predictive control with active damping in a direct matrix converter," in *Proc. 2009 IEEE Energy Conversion Congr. Expo.*, pp. 3057–3062.
[44] P. Cortes, J. Rodriguez, D. Quevedo, and C. Silva, "Predictive current control strategy with imposed load current spectrum," *IEEE Trans. Power Electron*, vol. 23, no. 2, pp. 612–618, Mar. 2008.
[45] H. Miranda, R. Teodorescu, P. Rodriguez, and L. Helle, "Model predictive current control for high-power grid-connected converters with output LCL filter," in *Proc. 2009 IEEE 35th Ann. Conf. Ind. Electron*, pp. 633–638.
[46] P. Lezana, R. Aguilera, and D. Quevedo, "Steady-state issues with finite control set model predictive control," in *Proc. 2009 IEEE 35th Ann. Conf. Ind. Electron*, pp. 1776–1781.
[47] R. Aguilera, P. Lezana, and D. Quevedo, "Finite-control-set model predictive control with improved steady-state performance," *IEEE Trans. Ind. Informat.*, vol. 9, no. 2, pp. 658–667, May 2013.

Niklas Panten was born in Aachen, Germany, on September 19, 1987. He received the B.Sc. and M.Sc. degrees in electrical engineering and business administration from the Christian-Albrechts-University of Kiel, Kiel, Germany, in 2012 and 2014, respectively. He is currently working toward the Ph.D. degree from the Institute for Production Management, Technology and Machine Tools (PTW), Technical University of Darmstadt, Darmstadt, Germany.

In 2011, he was an Intern at Delta Electronics (Shanghai) Co., Ltd., China, in the Automotive Development Department. In 2014, he was a Visiting Scholar at WEMPEC Research Group of the University of Wisconsin–Madison, USA. He is currently a Research Associate at the Institute for Production Management, Technology and Machine Tools (PTW), Technical University of Darmstadt. His current research interests include energy monitoring and power control strategies for energy efficiency in industrial production.

Nils Hoffmann (S'09–M'14) was born in Halle/Saale, Germany, in 1983. He received the Dipl.-Ing. and Dr.-Ing. degrees from the Christian-Albrechts-University of Kiel, Kiel, Germany, in 2009 and 2014, respectively.

Between 2009 and 2013, he was with the Institute of Power Electronics and Electrical Drives, Christian-Albrechts-University of Kiel, where he was involved in modern control strategies applied to grid-connected power converter systems. Since 2013, he has been with the Ingenieurbüro Hoffmann GmbH, Halle/Saale, Germany, where he is the Head of Research and Product Development for Power Electronics and Electrical Drives. He is involved in modern and innovative concepts of power electronic systems, electrical drives and renewable energy applications with the focus on technological consulting, assistance in problem cases, feasibility studies, preliminary and ready-to-release system designs, prototyping, and fundamental and advanced training services. His current research interests include the control of power converters and drives, power quality in distributed power generation networks, and modern multilevel converter topologies for high power adjustable speed drive applications.

Dr. Hoffmann is one of the recipients of the 2014 Best Paper Award of the German VDE Power Engineering Society. Further, his PhD thesis entitled "Grid-adaptive control and active-filter functionality of grid-connected PWM converters in renewable energy generation" was honored with the grade "summa cum laude" in 2014. He is an active Member of the IEEE Power Electronics Society, the IEEE Industrial Electronics Society, the IEEE Industry Applications Society, and the VDE Power Engineering Society.

Friedrich Wilhelm Fuchs (M'96–SM'01) received the Dipl.Ing. and Ph.D. degrees from the Rheinisch-Westfaelische Technische Hochschule (University of Technology), Aachen, Germany, in 1975 and 1982, respectively.

Between 1975 and 1982, he was with the University of Aachen, Aachen, where he was involved in research on ac automotive drives. From 1982 to 1991, he was a Group/Department Manager involved in research on the development of power electronics and electrical drives in a medium-sized company. In 1991, he became the Managing Director of the Converter and Drives Division (presently, GE Power Conversion), Allgemeine Elektrizitaets-Gesellschaft, Berlin, Germany, in the area of design and development of drive products, drive systems, and high power supplies (5 kVA to 50 MVA). In 1996, he joined the Christian-Albrechts-University of Kiel, Kiel, Germany, as a Full Professor and the Head of the Institute for Power Electronics and Electrical Drives. Since 2013 he is pensioned, but still very active in research project and phd managing. Prof. Liserre is his successor as head of the chair. Prof. Fuchs' research and that of his team include power semiconductor applications, converters topologies, and variable-speed drives as well as their control. Topics are research in renewable energy conversion, particularly wind and solar energy, their grid integration, ac electric drives for automobiles, nonlinear control of drives, and diagnosis of drives and fault-tolerant drives. Many research projects are carried out with industrial partners. Prof: Fuchs is the author or coauthor of more than 220 papers and one book chapter. He is Associate Editor of the IEEE TRANSACTION ON POWER ELECTRONICS and Convenor and International Speaker for the Standardization of Power Electronics (Deutsche Kommission Elektrotechnik Elektronik Informationstechnik (DKE), International Electrotechnical Commission), as well as a member of Verband der Elektrotechnik Elektronik Informationstechnik (VDE), European Power Electronics and Drives Association and IEEE.